Effects of Local Inhomogeneities on Tidal Strain Measurements

AUTHOR(S):

TAKEMOTO, Shuzo

CITATION:

TAKEMOTO, Shuzo. Effects of Local Inhomogeneities on Tidal Strain Measurements. Bulletin of the Disaster Prevention Research Institute 1981, 31(4): 211-237

ISSUE DATE:

1981-12

URL:

http://hdl.handle.net/2433/124905

Effects of Local Inhomogeneities on Tidal Strain Measurements

By Shuzo TAKEMOTO

(Manuscript received September 18, 1981)

Abstract

Using continuous records obtained from four extensometers with laser interferometer systems at Amagase, Kyoto Prefecture, we analyzed tidal strains by the least squares method. The result shows that there exist remarkable discrepancies between observed values and theoretically predicted ones for a laterally homogeneous earth model.

Amplitude enhancements of tidal strains observed with the horizontal and vertical components in normal directions to the axis of the tunnel are well explained by the cavity effects calculated by two-dimensional finite element techniques for the actual cross-section of the tunnel.

After eliminating the cavity effects, observed values were compared with theoretically predicted ones containing the topographic corrections calculated by three-dimensional finite element techniques. As a result, differences of phases between observed and theoretically predicted values are within 5° in any case. Amplitudes of observed tidal strains in the direction along the tunnel are about 15% smaller than predicted values but these differences are comparable to errors inherent in calculations. On the contrary, amplitudes of observed values in the direction across the tunnel are 33~52% larger than the predicted ones. As the most possible source of these differences, we consider the hydrological perturbation caused by fluctuations of the ground-water level around the observation tunnel.

1. Introduction

We have been carrying on ground-strain measurements using four extensometers with laser interferometer systems since 1978 at the Amagase Crustal Movement Observatory (Takemoto[1], hereafter referred to as Paper I). The development of extensometers with laser interferometer systems (e.g. Berger and Lovberg[2], Levine and Hall[3], Goulty et al.[4]) has increased the reliability of measurements of tidal strains, secular strains and low frequency seismic waves. However, for instance in tidal strain measurements, observational results obtained from these instruments are generally inconsistent with theoretically predicted values for a laterally homogeneous earth model.

As possible reasons for these discrepancies, effects of local inhomogeneities, i.e. cavity, topographic and geological inhomogeneities around the observation site, have been discussed by several authors. At first, concerning the effect of a cavity in which instruments are installed, King and Bilham[5] mentioned that underground cavities are deformed by the stress in the earth and that in particular, a cylindrical cavity is deformed by the horizontal compressive stress into an ellipsoidal cavity with the major axis of its cross-section aligned vertically. Itsueli et al.[6] confirmed this aspect from the tidal strain measurements at the Queensbury Observatory. According to their results, horizontal and vertical extensometers installed in the cross-section normal to the axis of the long tunnel showed large amplitudes as compared with the horizontal extensometers installed along the axis of the tunnel, and there

existed a good agreement between the predicted effect of a cylindrical cavity and the observed data. Similar observational results of tidal strain enhancements in other observatories have been reported by Ozawa[7] with the horizontal extensometer across the Osakayama tunnel and by Melchior et al.[8] with the vertical extensometer in the underground gallery at the Walferdange Observatory. Harrison[9] approximated the effects of cavities of more complicated shapes using analytical solutions for an ellipsoidal cavity and numerical calculations by two-dimensional finite element techniques for irregular shaped cavities. As a special case, Blair[10] estimated the "cavity effect" on the core hole strainmeter which was installed in a core hole drilled horizontally into surrounding rocks from an ellipsoidal cavity. In this case, he has noted that the local strain in the rock at a distance equal to the horizontal diameter of the cavity is reduced to a factor of one-half.

Secondly, the earth's surface cannot be assumed to be flat in the vicinity of the observation site. And the regional strain field, which is uniform in large scale, may be deformed by the local topography. Harrison[9] calculated effects of four different models of local topography by two-dimensional finite element techniques. He has found that the values of strains are large in the valley and small on the ground at the valley margins. Blair[10),11] also calculated the effect of the gorge structure near the Cooney Observatory by two-dimensional finite element techniques and confirmed this result using model experiments with a thin steel plate and strain gauges. Effects of more detailed topographic structures around the Cooney Observatory were estimated by Tanaka and Sydenham[12] by two-dimensional finite element techniques. Other approaches to estimating topographic effects using two-dimensional models were made by Emter et al.[13] for the Schiltach Observatory and by Ooe and Sato[14] for the Esashi Observatory. On the other hand, Levin and Harrison[15] and Berger and Beaumont[16] extended these calculations to include fully three-dimensional models. The former estimated the topographic effect for the Poorman Mine Observatory by three-dimensional finite element techniques and the latter similarly estimated those for six other observatories in the United States of America. Such an attempt of three-dimensional calculations was also made by Hashida and Shigetomi[17] for the Osakayama Observatory.

Thirdly, lateral inhomogeneities of elastic parameters caused by geological structures of various scales may also distort the regional homogeneous strain field. Latynina[18] pointed out that linear strains observed within a block bounded by deep fractures are extremely attenuated and on the contrary, those observed at the fractured boundary zone are strongly amplified. This assumption was confirmed by her and her co-workers from tidal strain observations carried on at the Kondarinsky fault zone and other fractured zones in the USSR (Latynina and Rizaeva[19], Latynina and Shishkina[20], Latynina[21]). Some possibilities of effects of small scale inhomogeneities around the observation tunnel were discussed by King[22], and King and Bilham[23]. In this respect, strong scatters of tidal strain amplitudes were observed with arrays of extensometers along axes of tunnels at the Queensbury Observatory and other temporal stations in Great Britain. These scatters were explained to be caused by variations of bulk and shear moduli along the arrays (Bilham et al.[24], Evans et al.[25]).

Many authors, previously referred to, have included geological inhomogeneities in their calculations of finite element models. However, as mentioned by Berger and

Beaumont[16], it is difficult to estimate geological effects by finite element techniques because the fine structure of the local geology is in general not well known. On the other hand, topographic and cavity effects are amenable to finite element techniques because the local topography and the shape of the cavity are available in perspicuous models.

The aim of this paper is to investigate the effects of local inhomogeneities on ground-strain measurements at the Amagase Observatory where four extensometers with laser interferometer systems were installed in a disused race tunnel having a length of 1830 m and thus quantitative measurements of ground-strains have been carried on (Paper I).

Using continuous records obtained from these extensometers for a period of 390 days, we analyzed tidal strains by the least squares method. The result shows that there exist remarkable discrepancies between observed and theoretically predicted amplitudes of tidal strains. In order to investigate these discrepancies, we calculated the effects of local inhomogeneities using two- and three-dimensional finite element techniques and compared these with observed values.

2. The Observational Results of Tidal Strains

Four extensometers with laser interferometer systems have been operating in the Amagase tunnel since 1978. The designs of these extensometers were described in detail in Paper I, therefore, only their general features are mentioned here.

The installation of instruments is shown in **Fig. 1**, together with the topographic map around the Amagase Observatory. EL–1 and EL–V components are super-invar bar extensometers with laser interferometer systems, each of which consists of a simple (unstabilized) laser source, the Michelson interferometer and a photo-detecting equipment with an image-sensor. L–1 and L–2 components are laser extensometers with a frequency-stabilized laser source and mutually perpendicular evacuated light paths. EL–1 and L–1 components are orientated along the axis of the tunnel and the L–2 component is across the tunnel. The EL–V is a vertical component. Resolving powers and other numerical constants of these instruments are given in **Table 1**. Examples of ground-strain records for a period of a fortnight are shown in **Fig. 2**, together with barometric and thermometric records. In this figure, tidal strain amplitudes obtained from L–2 and EL–V are extremely larger than those obtained from L–1 and EL–1. This can be considered to be due to the cavity effect. We will discuss this respect in the following section.

Table 1. Constants of laser extensometers at the Amagase Observatory (34°53′N, 135°50′E).

Mark	Azimuth	Span	Resolving Power
L–1	N72.5°W	15.8 m	1.0×10^{-9} strain
L–2	N17.5°E	3.2 〃	5.0 〃
EL–1	N72.5°W	40.0 〃	0.25 〃
EL–V	Vertical	6.4 〃 *	1.5 〃

* total length containing standard bar and concrete base.

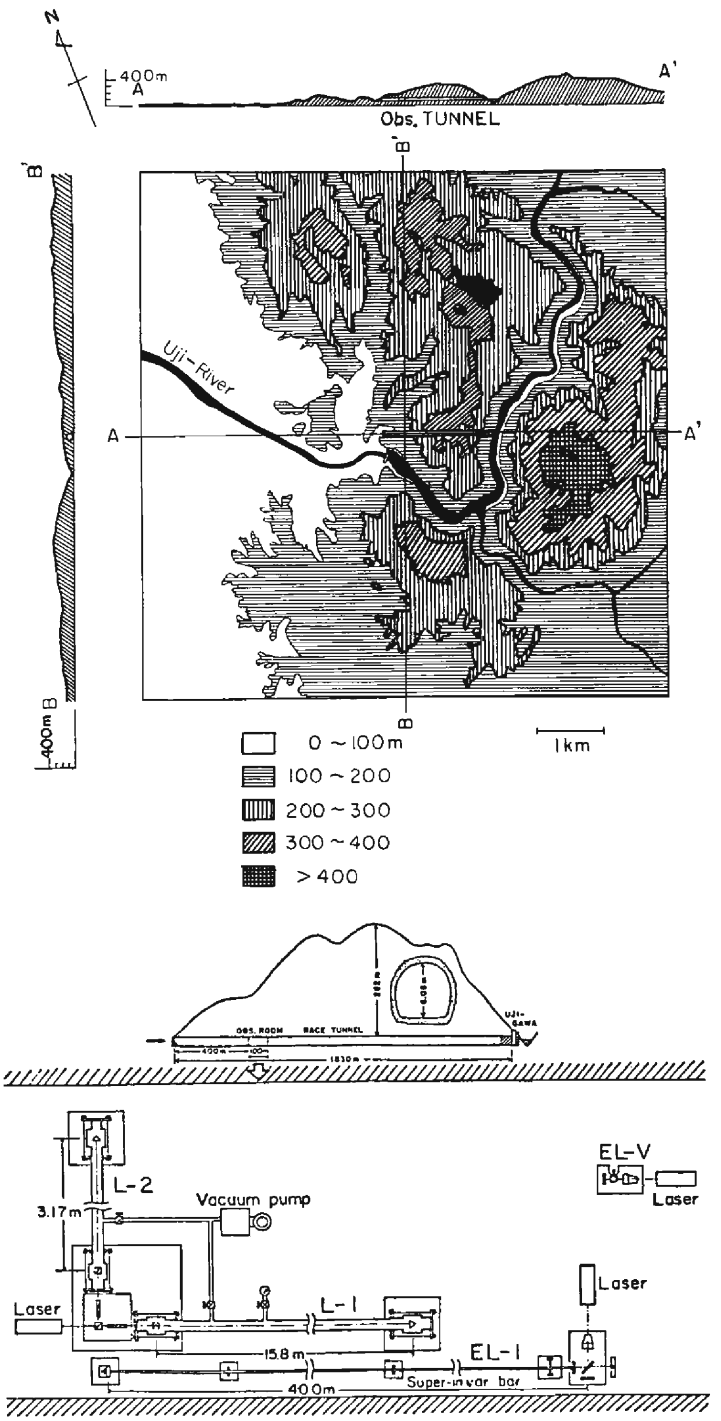

Fig. 1. Topographic map around the Amagase Observatory (upper) and installation of instruments (lower).

Tidal strains were analyzed using continuous records of these four extensometers for the period from March 06 1979 to March 31 1980. At first, drifts were eliminated by applying the Pertzev's filter, then, amplitudes and phase lags of 12 major tidal constituents were determined by applying the least squares method to the drift-eliminated data for the sampled time interval of 8856 hours (369 days). The 20 times analyses were successively repeated by shifting the time interval every 24 hours. Mean values of amplitudes and phase lags obtained from these analyses are given in **Table 2**, together with mean squares errors.

Comparing amplitudes of 12 constituents obtained from EL–1 and L–1 extensometers installed in the parallel direction at adjacent positions, there are systematic discrepancies between them; results obtained from the former are about 30% smaller than those obtained from the latter. It may be caused by frictional forces between the super-invar bar and its supporting rollers (Paper I). L–1 and L–2 components are free from these frictional forces because "length standards of solid materials" such as super-invar bars are not used in their systems but evacuated light paths are used as length standards. The EL–V component is also free from frictional forces because the length standard of super-invar bar in this system is not supported by any intermediate fittings. Therefore, in following discussions only L–1, L–2 and EL–V components are used.

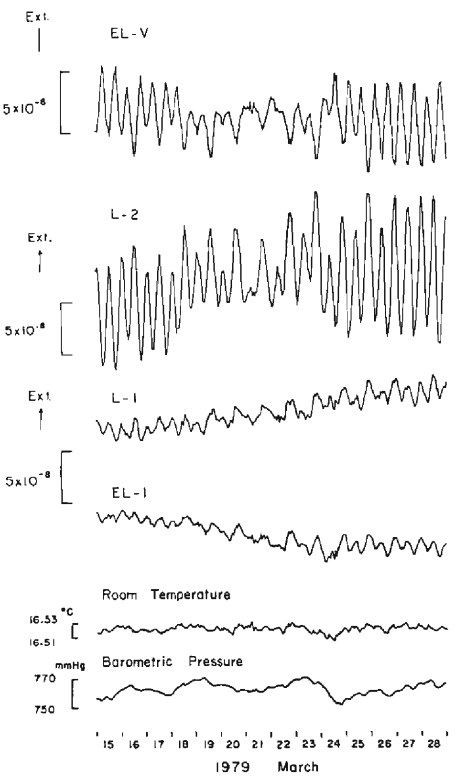

Fig. 2. Examples of records obtained from laser extensometers, together with thermometric and barometric records for a period of a fortnight.

Table 2. Amplitudes and phase lags of 12 major constituents obtained by least squares method.

	EL–1		L–1		L–2		EL–V	
	Amplitude ($\times 10^{-9}$)	Phase lag (degree)	Amplitude ($\times 10^{-9}$)	Phase lag (degree)	Amplitude ($\times 10^{-9}$)	Phase lag (degree)	Amplitude ($\times 10^{-9}$)	Phase lag (degree)
Q_1	0.631	15.66	0.764	15.69	2.577	−47.14	1.244	138.93
	±0.001	±0.34	±0.002	±0.34	±0.007	±0.25	±0.005	±0.35
O_1	3.043	12.30	4.211	11.55	15.225	−16.24	7.467	169.52
	±0.002	±0.06	±0.002	±0.04	±0.015	±0.05	±0.007	±0.04
M_1	0.364	−13.53	0.402	−16.55	0.814	−148.09	0.431	71.20
	±0.001	±0.42	±0.002	±0.21	±0.007	±0.64	±0.004	±0.86
P_1	1.426	20.08	2.330	27.70	17.011	−42.45	7.778	142.87
	±0.001	±0.08	±0.004	±0.04	±0.012	±0.16	±0.005	±0.15
S_1	1.100	173.53	0.716	114.66	7.551	−39.21	4.883	146.15
	±0.002	±0.08	±0.004	±0.13	±0.049	±0.04	±0.021	±0.06
K_1	3.313	20.00	4.901	21.49	28.695	−10.33	14.433	174.39
	±0.002	±0.02	±0.004	±0.03	±0.032	±0.07	±0.017	±0.06
J_1	0.288	16.99	0.253	41.71	3.102	−51.17	1.397	127.58
	±0.001	±0.21	±0.001	±0.44	±0.013	±0.10	±0.011	±0.14
N_2	0.730	−7.82	1.036	−11.22	6.392	8.78	3.043	−167.19
	±0.001	±0.14	±0.001	±0.21	±0.007	±0.15	±0.007	±0.14
M_2	3.558	−2.80	5.052	−3.93	35.562	7.15	16.312	−169.98
	±0.002	±0.03	±0.003	±0.04	±0.014	±0.03	±0.009	±0.03
S_2	1.034	−62.52	1.781	3.19	16.678	−13.72	9.733	175.34
	±0.001	±0.09	±0.005	±0.04	±0.008	±0.03	±0.004	±0.04
K_2	0.241	−3.66	0.460	4.81	3.549	13.11	1.586	−158.54
	±0.001	±0.40	±0.005	±0.08	±0.009	±0.10	±0.002	±0.20
S_3	0.223	−132.94	0.044	−108.01	1.263	80.37	0.740	−132.67
	±0.001	±0.28	±0.002	±3.66	±0.002	±0.15	±0.002	±0.20

3. Elimination of the Cavity Effect from Observational Results

3.1 Cavity Effect around a Cylindrical Cavity

For the first approximation, we consider strain changes around the cylindrical cavity in an infinite homogeneous isotropic elastic medium in which the strain would be uniform in the absence of the cavity. We shall use a rectangular coordinate system in which x and y axes are in the horizontal plane and the z axis is normal to this plane. We assume that the cavity has an equal cross-section in the x direction.

The three dimensional state of stress is defined by specifying the magnitudes of the three components of normal stresses (σ_x, σ_y, σ_z) and the three components of shearing stresses (τ_{xy}, τ_{yz}, τ_{zx}). Among them, σ_z, τ_{yz} and τ_{zx} should vanish if the condition of the free surface can be applied. The depth at which our instruments are buried is much less than the wavelengths of tidal strains. Major et al.[26] show that tidal strains observed at this approximate depth do not differ significantly from

those observed at the earth's surface. This condition is perturbed by the topographic effect. But as shown in the following section, the normal stress σ_z induced by the topographic effect is negligibly small (less than 4%). We thus adopt the condition of free surface,

$$\sigma_z=0, \quad \tau_{yz}=\tau_{zx}=0. \tag{1}$$

According to Panek[27], the shearing stress which acts parallel to the axis of the cavity has negligible influence on the strain change in the cross-section of the cavity. Therefore,

$$\tau_{xy}=0. \tag{2}$$

Consequently, strain changes around the cavity is a function only of σ_x and σ_y. The stresses and strains are the same in any slice of unit thickness normal to the axis of the cavity. We use the notation $(e^0_{xx}, e^0_{yy}, e^0_{zz})$ for linear strains which should be observed in the absence of the cavity and $(e^c_{xx}, e^c_{yy}, e^c_{zz})$ for those around the cavity.

General equations of stress-strain relations in the absence of the cavity can be written as follows,

$$e^0_{xx}=(1/E)\,(\sigma_x-\nu\sigma_y), \tag{3}$$
$$e^0_{yy}=(1/E)\,(\sigma_y-\nu\sigma_x), \tag{4}$$
$$e^0_{zz}=(-\nu/E)\,(\sigma_x+\sigma_y), \tag{5}$$

where E is the Young's modulus and ν is the Poisson's ratio. Equations (4) and (5) can be rewritten as follows,

$$e^0_{yy}=[(1-\nu^2)/E]\sigma_y-[\nu/E](\sigma_x-\nu\sigma_y), \tag{6}$$
$$e^0_{zz}=[-\nu(1+\nu)/E]\sigma_y-[\nu/E](\sigma_x-\nu\sigma_y). \tag{7}$$

In these equations ((6), (7)), the first terms of the right side are strain changes due to the normal stress σ_y under the plane strain condition ($e^0_{xx}=0$) and the second terms are additional strains induced by the strain e^0_{xx} along the axis of the cavity. Substituting Eq. (3) into Eqs. (6) and (7), we obtain the following reduced forms,

$$e^0_{yy}=a\sigma_y-\nu e^0_{xx}, \tag{8}$$
$$e^0_{zz}=b\sigma_y-\nu e^0_{xx}, \tag{9}$$

where $a=[(1-\nu^2)/E]$ and $b=[-\nu(1+\nu)/E]$.

Similarly, e^c_{yy} and e^c_{zz} can be expressed as follows,

$$e^c_{yy}=a'\sigma_y-\nu e^c_{xx}, \tag{10}$$
$$e^c_{zz}=b'\sigma_y-\nu e^c_{xx}. \tag{11}$$

The strain component along the axis of the cavity is not affected by the existence of the cavity. Then,

$$e^c_{xx}=e^0_{xx}. \tag{12}$$

Coefficients a' and b' in Eqs. (10) and (11) are analytically determined if the shape of the cavity is a simple form. For circular (cylindrical) cavity, Sokolnikoff[28]

gives the solution for the radial displacement U due to a stress σ_y under the condition of the plane strain:

$$U=[(1-\nu^2)R/E](1+2\cos 2\theta)\sigma_y, \tag{13}$$

where R is the radius of the circular cavity and θ is the angle with respect to y measured in $y-z$ plane. Using this result, a' and b' are expressed as follows,

$$a'=3\times[(1-\nu^2)/E],$$
$$b'=-1\times[(1-\nu^2)/E].$$

Putting $A=a'/a$ and $B=b'/a$, and referring to Eq. (12), e^c_{yy} and e^c_{zz} are expressed as functions of e^0_{xx} and e^0_{yy} as follows,

$$e^c_{yy}=A(e^0_{yy}+\nu e^0_{xx})-\nu e^0_{xx}, \tag{14}$$
$$e^c_{zz}=B(e^0_{yy}+\nu e^0_{xx})-\nu e^0_{xx}. \tag{15}$$

For the case of the circular cavity, substituting $A=3.0$ and $B=-1.0$, Eqs. (14) and (15) can be expressed as follows,

$$e^c_{yy}=3.0e^0_{yy}+2.0\nu e^0_{xx}, \tag{16}$$
$$e^c_{zz}=-(e^0_{yy}+2.0\nu e^0_{xx}). \tag{17}$$

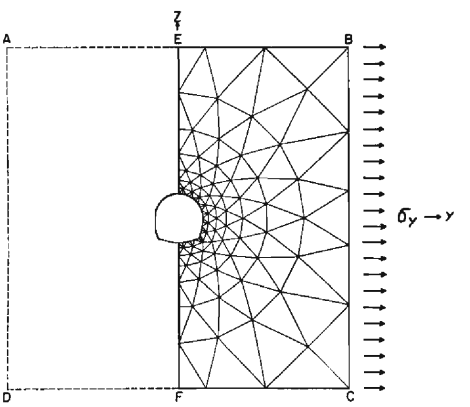

Fig. 3. Finite element grid used for calculations of cavity effects.

3.2 Cavity Effect Calculated by the Two-Dimensional Finite Element Method

The cross-section of real tunnel at Amagase is not a circular but a horseshoe shape and it is difficult to obtain analytical solutions for its deformations. Therefore, finite element calculations were made to illustrate the strain change around the actual cavity. Procedures of computations were referred to Zeinkiewicz[29] and the plane strain condition was postulated.

As shown in **Fig. 3**, a large square plate ABCD has a cavity at its center. The dimension of the plate is about 7 times that of the cavity. Uniform pressures, which would produce uniform strains in the absence of the cavity, are applied to the

faces AD and BC. Faces AB and CD are free. The mirror image symmetry is assumed about the line EF, so that calculations are made only for the half-plate EBCF, which is divided into 161 elements with 104 nodes. Along the line EF, nodal displacements of the y direction are fixed to be zero.

In order to evaluate the accuracy of calculations, we initially calculated nodal displacements around the circular cavity and compared the values of A and B, defined in the previous subsection, with those obtained analytically. As a result, the values of A calculated with the finite element method varied between 2.88 and 2.96 and that of B varied between -0.97 and -1.02. Comparing these values with analytical ones ($A=3.0$ and $B=-1.0$), deviations are within the 4%. Then, we calculated the values of A and B for the actual cross-section of the Amagase tunnel. Results with a Poisson's ratio of 0.25 are shown in **Fig. 4**. At the place where the instruments were installed, the values of A and B are obtained to be 2.44 and -0.92, respectively. Relations between (e^c_{yy}, e^c_{zz}) and (e^0_{xx}, e^0_{yy}) in this case are expressed as follows,

$$e^c_{yy}=2.44e^0_{yy}+1.44\nu e^0_{xx}, \tag{18}$$

$$e^c_{zz}=-(0.92e^0_{yy}+1.92\nu e^0_{xx}). \tag{19}$$

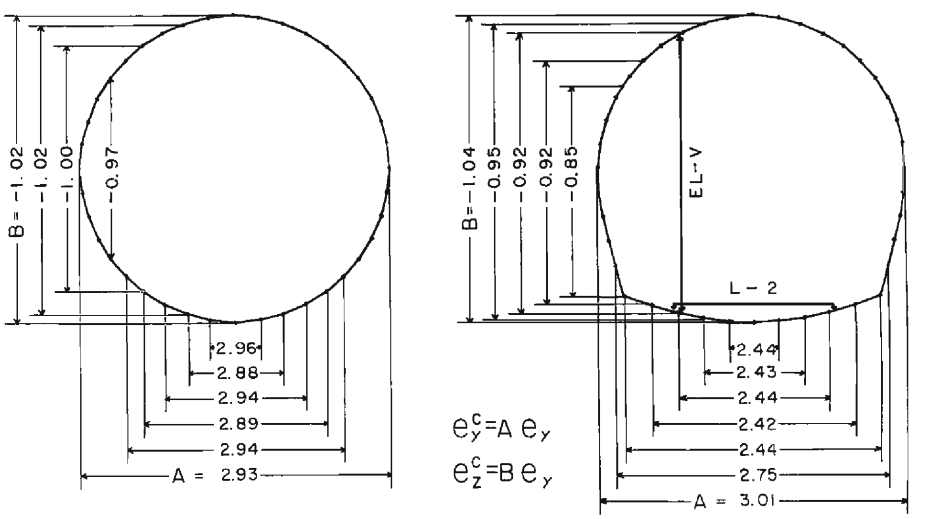

Fig. 4. Cavity effects obtained from finite element techniques for two cases of the circular profile (left) and the actual tunnel profile (right).

Equations (14) and (15) are expressions connecting strain components around the cavity (e^c_{yy} and e^c_{zz}) with those in the absence of the cavity (e^0_{xx} and e^0_{yy}) using coefficients A and B. These coefficients are not determined explicitly from these equations because the amount of e^0_{yy} is unknown. Using Eq. (12), we rewrite Eqs. (14) and (15) as follows,

$$e^c_{yy}+\nu e^c_{xx}=A(e^0_{yy}+\nu e^0_{xx}), \tag{20}$$

$$e^c_{zz}+\nu e^c_{xx}=B(e^0_{yy}+\nu e^0_{xx}). \tag{21}$$

From these equations, we obtain,

$$(e^c_{yy}+\nu e^c_{xx})/(e^c_{zz}+\nu e^c_{xx})=A/B. \tag{22}$$

This equation does not involve the unknown e^0_{yy}, so we can thus determine the ratio of A and B by substituting the observed values of e^c_{xx}, e^c_{yy} and e^c_{zz} into Eq. (22).

Now, tidal strains are periodic functions and so we can use the following expressions instead of Eqs. (20) and (21);

$$e^c_{yy}+\nu e^c_{xx}=|A|k\cos D, \tag{23}$$

$$e^c_{zz}+\nu e^c_{xx}=|B|k\cos(D-\delta). \tag{24}$$

Substituting observed values of tidal strains obtained from L–1, L–2 and EL–V components into Eqs. (23) and (24), the values of $|A|/|B|$ and δ were determined. The Poisson's ratio was assumed to be 0.279 with velocities of P and SV waves ($V_p=4.4_6$ km/sec and $V_s=2.5_8$ km/sec[30]). Results are shown in **Table 3**. Values of $|A|/|B|$ and δ for M_2, K_1, O_1, P_1, N_2, Q_1, K_2 and J_1 constituents are within the range of 2.2~2.5 and 172°~190°, respectively. For S_2, S_1, M_1 and S_3 constituents, values of $|A|/|B|$ are fairly small. Deviations existing in cases of S_2 and S_1 constituents may be influenced by atmospheric and thermometric perturbations in the tunnel. In cases of M_1 and S_3 constituents, we cannot discuss the results in detail because their amplitudes are extremely small.

Table 3. $|A|/|B|$ and phase lag δ defined by equations (23) and (24).

Constituent	$\lvert A\rvert/\lvert B\rvert$	Phase lag (degree)
M_2	2.473	184.60
K_1	2.258	180.62
O_1	2.548	179.86
P_1	2.292	178.78
S_2	1.857	188.15
N_2	2.397	187.32
Q_1	2.350	172.98
S_1	1.458	183.49
K_2	2.513	190.09
M_1	1.655	−161.69
J_1	2.208	174.56
S_3	1.665	147.27

The theoretical value of A/B is −3.0 for the circular cavity and −2.65 for the actual horseshoe shaped cavity. The latter gives fairly good agreement with observed values of −2.2~−2.5.

Substituting the value of A into Eq. (20) or B into Eq. (21), the value of e^0_{yy} can be determined by observed values of e^c_{xx}, e^c_{yy} and e^c_{zz}. Here we use the notation $e^0_{yy}(1)$ for the value of e^0_{yy} obtained from Eq. (20) and $e^0_{yy}(2)$ for that obtained from Eq. (21). Values of $e^0_{yy}(1)$ and $e^0_{yy}(2)$ ought to be the same, but as shown in **Table 4**,

the former is in some degree smaller than the latter in any case of 12 constituents. The most possible reason for this significant difference can be considered to be that our estimation of the "effective length" of the vertical extensometer is not suitable, i.e. we have so far considered that the "effective length" of the vertical extensometer at the Amagase tunnel is consistent with the total height measured from the bottom of the concrete base to the ceiling of the tunnel at which the upper end of the super-invar bar is fixed. However, it may be true that the "effective length" of the vertical extensometer, which is installed in the horizontal tunnel, is to some extent larger than the total height measured from the floor to the ceiling of the tunnel. Melchior et al.[8] adopted the "effective length" of 3.4 m for the vertical extensometer installed in the gallery of the total height of 3 m at the Walferdange Observatory. In our case, if the value of the "effective length" of the EL–V component is 10% larger than that of the total height (given in **Table 1**), $e^0_{yy}(2)$ becomes approximately consistent with $e^0_{yy}(1)$. In this respect, more detailed discussions will be made in the future. At the present time, we use only $e^0_{yy}(1)$ as the strain component e^0_{yy} of the y direction in the absence of the cavity.

Table 4. Tidal strains in the y direction eliminated for the cavity effect.

$e^0_{yy}(1)$; obtained from Eq. (20),
$e^0_{yy}(2)$; obtained from Eq. (21).

Constituent	$e^0_{yy}(1)$		$e^0_{yy}(2)$	
	Amplitude ($\times 10^{-9}$)	Phase lag (degree)	Amplitude ($\times 10^{-9}$)	Phase lag (degree)
M_2	13.756	7.82	14.882	12.76
K_1	11.080	−12.54	13.203	−11.28
O_1	5.634	−19.54	5.908	−19.47
P_1	6.851	−45.48	7.971	−46.02
S_2	6.554	−14.47	9.549	−5.51
N_2	2.459	10.14	2.766	17.92
Q_1	1.005	−53.56	1.169	−59.70
S_1	3.201	−40.14	5.669	−36.06
K_2	1.379	13.57	1.468	24.47
M_1	0.381	204.41	0.532	225.03
J_1	1.274	−53.05	1.536	−57.93
S_3	0.525	80.25	0.828	48.07

Table 5. Observed tidal strains normalized with nodal parameters of the moon.

	M_2 constituent		O_1 constituent	
	Amplitude ($\times 10^{-9}$)	Phase lag (degree)	Amplitude ($\times 10^{-9}$)	Phase lag (degree)
e^0_{xx}	4.88	−3.9	5.11	11.6
e^0_{yy}	13.29	7.8	6.84	−19.5

Values for e^0_{yy} are previously corrected with the cavity effect.

For M_2 and O_1 constituents, e^0_{xx} and e^0_{yy} are compared with theoretically expected values at the Amagase Observatory. The values of e^0_{xx} and e^0_{yy} normalized with nodal parameters of the moon (f and u) are given in **Table 5**.

4. Theoretically Expected Tidal Strains at Amagase

4.1 Bodily Tide

The tide generating potential W_2 of second order at the earth's surface can be expressed as follows for M_2 and O_1 constituents, respectively;

$$W_2(M_2)=DC_1 \sin^2\theta \cos(2T+u), \tag{25}$$
$$W_2(O_1)=DC_2 \sin 2\theta \cos(T'+u'), \tag{26}$$

where D is the tidal constant of Doodson, C_1 and C_2 are factors containing the declination of the moon and θ is the colatitude of the observation site. The numerical value of D is referred to Melchior[31] as follows,

$$D=2.627723\, m^2/\mathrm{sec}^2.$$

C_1 and C_2 are expressed in terms of the eccentricity e of the lunar orbit and the inclination I of the lunar orbit on the equator (Nakano[32]),

$$C_1=(1-5/2\times e^2)\cos^4(I/2),$$
$$C_2=(1-5/2\times e^2)\sin I\cos^2(I/2).$$

Owing to the slow revolution of the nodes of the lunar orbit, C_1 and C_2 vary slowly (one cycle per 18.61 years) and as the result we prefer in practice to introduce $\bar{C}_1$ and $\bar{C}_2$ instead of C_1 and C_2. Where $\bar{C}_1$ and $\bar{C}_2$ are mean values of C_1 and C_2, respectively;

$$\bar{C}_1=(1-5/2\times e^2)[\overline{\cos^4(I/2)}][\overline{\cos u}]=0.9085,$$
$$\bar{C}_2=(1-5/2\times e^2)[\overline{\sin I\cos^2(I/2)}][\overline{\cos u'}]=0.3771.$$

The procedure for these numerical constants is described in detail by Nakano[32]. Substituting these values into Eqs. (25) and (26), we obtain the following expressions for W_2 (M_2) and W_2 (O_1).

$$W_2(M_2)=2.3873\times\sin^2\theta\cos(2T+u), \tag{27}$$
$$W_2(O_1)=0.9910\times\sin 2\theta\cos(T'+u'). \tag{28}$$

Three independent components of tidal strains at the surface of the earth can be expressed in terms of W_2 in the spherical coordinate system with the colatitude θ and the longitude λ measured in the east direction from Greenwich;

$$e_{\theta\theta}=\frac{l}{gr}\frac{\partial^2 W_2}{\partial\theta^2}+\frac{h}{gr}W_2,$$
$$e_{\lambda\lambda}=\frac{l}{gr\sin^2\theta}\frac{\partial^2 W_2}{\partial\lambda^2}+\frac{l}{gr}\frac{1}{\sin\theta}\cos\theta\frac{\partial W_2}{\partial\theta}+\frac{h}{gr}W_2, \tag{29}$$

$$e_{\theta\lambda}=\frac{2l}{gr\sin\theta}\frac{\partial^2 W_2}{\partial\theta\partial\lambda}-\frac{2l}{gr\sin\theta}\cot\theta\frac{\partial W_2}{\partial\lambda},$$

where g is the local acceleration of gravity, r is the radius of the earth, h and l are Love and Shida numbers, respectively. Numerical values at present used are,

$$\begin{aligned}
&g=9.797\ m/\mathrm{sec}^2\\
&r=6.371\times10^6\ m\\
&h=0.6114\ (\text{referred to Farrell}^{33})\\
&l=0.0832\ (\qquad\quad''\qquad\quad)\\
&\theta=55°07'\\
&\lambda=135°50'.
\end{aligned}$$

Substituting these values into Eqs. (29), the following expressions can be obtained; for the M_2 constituent,

$$\begin{aligned}
e_{\theta\theta}&=3.825\times10^{-8}\ (h\sin^2\theta+2l\cos2\theta)\cos(2T+u),\\
e_{\lambda\lambda}&=3.825\times10^{-8}\ \{h\sin^2\theta-2l(1+\sin^2\theta)\}\cos(2T+u),\\
e_{\theta\lambda}&=3.825\times10^{-8}\ (-4l\cos\theta)\sin(2T+u),
\end{aligned}\tag{30}$$

$$\begin{aligned}
e_{\theta\theta}&=13.53\times10^{-9}\cos(2T+u),\\
e_{\lambda\lambda}&=\ 5.09\times10^{-9}\cos(2T+u),\\
e_{\theta\lambda}&=-7.27\times10^{-9}\sin(2T+u),
\end{aligned}\tag{30}'$$

for the O_1 constituent,

$$\begin{aligned}
e_{\theta\theta}&=1.588\times10^{-8}(h-4l)\sin2\theta\cos(T'+u'),\\
e_{\lambda\lambda}&=1.588\times10^{-8}(h-2l)\sin2\theta\cos(T'+u'),\\
e_{\theta\lambda}&=1.558\times10^{-8}(4l\sin\theta)\sin(T'+u'),
\end{aligned}\tag{31}$$

$$\begin{aligned}
e_{\theta\theta}&=4.16\times10^{-9}\cos(T'+u'),\\
e_{\lambda\lambda}&=6.63\times10^{-9}\cos(T'+u'),\\
e_{\theta\lambda}&=4.33\times10^{-9}\sin(T'+u').
\end{aligned}\tag{31}'$$

Eqs. (30)' and (31)' are transformed into the rectangular coordinate system with the directions x along the tunnel (N107.5°E) and y across the tunnel (N17.5°E). In the following discussions, we use the definition of $e_{xy}=1/2\times(\partial v/\partial x+\partial u/\partial y)$ instead of $e_{xy}=(\partial v/\partial x+\partial u/\partial y)$ for convenience of expressing strain components with a tensor. For the M_2 constituent, we obtain,

$$\begin{aligned}
e_{xx}&=6.21\times10^{-9}\cos\{(2T+u)+19.6°\},\\
e_{yy}&=12.94\times10^{-9}\cos\{(2T+u)-9.3°\},\\
e_{xy}&=3.84\times10^{-9}\cos\{(2T+u)-129.2°\},
\end{aligned}\tag{32}$$

and for the O_1 constituent,

$$e_{xx}=6.53\times10^{-9}\cos\{(T'+u')-11.0°\},$$

$$e_{yy}=4.56\times10^{-9}\cos\{(T'+u')+15.8°\},$$
$$e_{xy}=1.91\times10^{-9}\cos\{(T'+u')+68.2°\}. \tag{33}$$

4.2 Loading Effects of Ocean Tides

The loading effects of ocean tides can be calculated by convolving the complex amplitude of the ocean tide with the Green's function. The convolution integral can be written in the form,

$$\mathbf{e}(\mathbf{r})=\rho g\iint_{\text{oceans}}\mathbf{H}(\mathbf{r}')\mathbf{G}(\mathbf{r}-\mathbf{r}')\,dA\,, \tag{34}$$

where ρ is the density of the sea water, g is the acceleration of gravity, $\mathbf{r}$ and $\mathbf{r}'$ are vectors describing the positions of the observation site and the water mass load, respectively. The green's functions (**G**) for surface mass loadings were obtained by Farrell[33] for three gravitating and radially stratified earth models. Among them, values of **G** for the Gutenberg-Bullen A earth model were employed in our calculations.

In both cases of M_2 and O_1 constituents, the complex amplitudes of ocean tides were determined with the co-tidal and co-range charts given by Ogura[34] for local tides in the seas adjacent to Japan and with charts of ocean tides given in the *ATAAC OKEAHOB*[35),36] for global tides in the rest of the world oceans. To perform calculations, seas and oceans were divided into a number of meshes surrounded by latitudes and longitudes. Their dimensions were $0.1°\times0.1°\sim1°\times1°$ in regions within $25°\sim55°$N and $120°\sim145°$E, and $5°\times5°\sim10°\times10°$ in the rest of the world oceans. We assumed that the height and phase of ocean tide were constant everywhere in each mesh and the distributed load in this element was substituted by a concentrated load at its center. Land areas were assigned a zero height. The total loading effect was approximated by summing up all of contributions from each element using a linear interpolation from the Farrell's table of the Green's function. Results are shown in **Table 6**.

The reliability of these estimations of loading effects is considered to depend mainly on the accuracy of assumed height and phase of the ocean tide. In order to examine this point, we compared our results for the M_2 constituent with those obtained independently by Tanaka and Hashida (personal communications). They used the tidal chart of Hendershott[37] for modelling complex amplitudes of global tides. For local tides in the seas adjacent to Japan, they also used the tidal chart given by Ogura[34] but were different in manners of dividing oceans and seas into grid elements. In **Fig. 5**, our results are shown with the mark ①, and those of Tanaka and Hashida are shown with marks ② and ③, respectively. There are fairly good agreements between three independent calculations and differences are within 0.7×10^{-9} in amplitude and 14° in phase.

The sum of bodily tides (i.e. theoretical tidal strains for a solid earth (**E**)) and contributions from loading effects of ocean tides (**L**) were defined as the homogeneous tidal strains (**H**) by Beaumont and Berger[38]. Values of **E**, **L** and **H** expected for M_2 and O_1 constituents at the Amagase Observatory are given in **Table 6**. Values in the x direction were previously reported in Paper I (p. 78, Table 1), but they contained some calculation errors. Therefore, we show corrected values in **Table 6**.

Table 6. Theoretical tidal strain expected at the Amagase Observatory.

	M_2 constituent		O_1 constituent	
	Amplitude ($\times 10^{-9}$)	Phase lag (degree)	Amplitude ($\times 10^{-9}$)	Phase lag (degree)
x-direction (N72.5°W)				
E	6.21	−19.6	6.53	11.0
L	1.90	64.6	0.52	77.8
H	6.67	−3.2	6.75	15.0
y-direction (N17.5°E)				
E	12.94	9.3	4.56	−15.8
L	2.81	−153.4	0.29	−84.5
H	10.29	4.6	4.67	−19.1

E: Theoretical tidal strain for the Gutenberg-Bullen A earth model.
L: Contribution from the ocean tide loading.
H: Homogeneous tidal strain (=**E**+**L**).

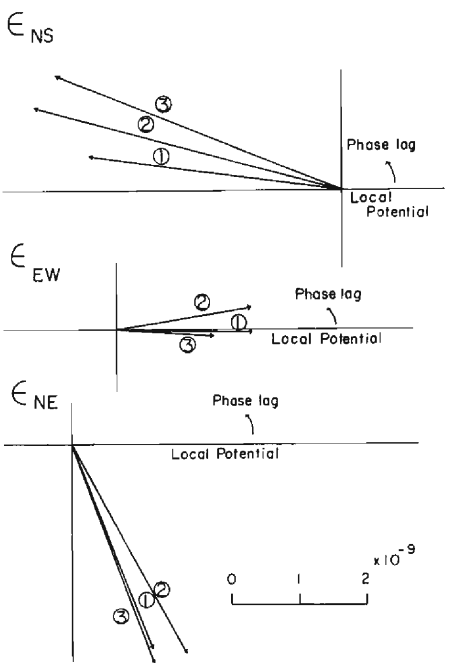

Fig. 5. Comparison of loading effects **L** calculated for Amagase using different tidal charts of oceans,
①; our results used in this paper,
②; results of Tanaka,
③; results of Hashida.

Comparing e^0_{xx} and e^0_{yy} shown in **Table 5** with homogeneous tidal strains (**H**), there exist systematic discrepancies between them; e^0_{xx} is smaller than **H** and e^0_{yy} is larger than **H** in each case of M_2 and O_1 constituents. We will examine in the following sections whether these discrepancies can be explained by the effect of local topography around the observatory.

5. Topographic Effects

At the stress-free surface of a half-space, there are only three independent strain components of $e_1=e_{xx}$, $e_2=e_{xy}$ and $e_3=e_{yy}$. We assume that the regional homogeneous strain e_j is transformed into e^t_i due to the effect of local topography. This transformation can be written as follows similar to that of Berger and Beaumont[16],

$$e^t_i=[T_{ij}]e_j \tag{35}$$

where $[T_{ij}]$ is the transformation matrix of the topographic effect. For instance, T_{11} is the term multiplying an applied strain e_1 in the x direction to obtain the perturbed strain e^t_1 in the same direction. Similarly, T_{21} and T_{31} are those to obtain the induced shear strain e^t_2 and linear strain e^t_3. Each term of $[T_{ij}]$ is estimated by the three-dimensional finite element technique, the procedure of which is referred to Zeinkiewicz[29].

In finite element calculations, a continuous medium is replaced by a finite number of elements which are interconnected only at a finite number of nodal points. Basic unknowns of the system are the nodal point displacements $\{\boldsymbol{\delta}\}$ under applied forces $\{\mathbf{f}\}$ on the nodal points. The $\{\boldsymbol{\delta}\}$ and $\{\mathbf{f}\}$ are linked by the stiffness matrix $[\mathbf{K}]$ as follows,

$$\{\mathbf{f}\}=[\mathbf{K}]\{\boldsymbol{\delta}\}. \tag{36}$$

In each element, we assume the displacement function such that internal continuity and compatibility between adjacent elements across common boundaries are assured. Based on this assumption, the strain and stress distributions in the element can be expressed implicitly as functions of nodal point displacements $\{\boldsymbol{\delta}\}$. The element stiffness matrix $[\mathbf{k}]$ is formed by integrating the matrix product $\mathbf{B^TDB}$ over the element volume. Here **B** and **D** are the strain-displacement and stress-strain matrices, respectively. That is,

$$[\mathbf{k}]=\int_v \mathbf{B^TDB}\,dV. \tag{37}$$

The stiffness matrix $[\mathbf{K}]$ of the complete structure can be formed by systematic additions of $[\mathbf{k}]$ of all elements. Then, unknown displacements of nodal points are determined by solving the stiffness equation (36).

Practically, the number of elements is limited by the capacity of the available computer. In our calculation using FACOM M-160AD, 484 elements are used. The model of continuous structure is divided into four layers, each of which is subdivided into 121 (11×11) elements in the x-y plane where grids are rectangular and increase in size toward the perimeter of the model. The topography is represented by specifying the height of each nodal point at the free surface. With increasing

depth into the model, the relative heights of nodal points are progressively smoothed.

As shown in **Fig. 6**, a typical element is an inclined hexahedron having eight nodes, each of which has three degrees of freedom (u_x, u_y, u_z). Here we introduce the local skew coordinate system (ξ, η, ζ), instead of the global rectangular coordinate system (x, y, z). There exists one-to-one correspondence between (x, y, z) and (ξ, η, ζ). Values of ξ are normalized to be -1 and $+1$ on the plane faces of 1, 2, 5, 6 and 3, 4, 7, 8, respectively. Similar normalizations are made for η and ζ on corresponding plane faces shown in **Fig. 6** (upper). In this normalized coordinate system, the simplest expression of the displacement function for an eight-noded hexahedron can be given as follows,

$$u_x=\alpha_1+\alpha_2\xi+\alpha_3\eta+\alpha_4\zeta+\alpha_5\xi\eta+\alpha_6\eta\zeta+\alpha_7\zeta\xi+\alpha_8\xi\eta\zeta \tag{38}$$

and similarly for u_y and u_z. The number of terms in series of Eq. (38) are chosen to be equal to the total number of nodal points and the coefficients $\alpha_1\sim\alpha_8$ can be expressed in terms of eight nodal displacements ($u_{x_1}\sim u_{x_8}$). Element strains are defined as appropriate derivatives of assumed displacement functions in the global coordinate (x, y, z). Therefore, it is necessary to transform these from (x, y, z) into (ξ, η, ζ). Transformations are made by using the jacobian matrix [**J**] expressed as the following form,

$$\begin{bmatrix} \dfrac{\partial}{\partial\xi} \\ \dfrac{\partial}{\partial\eta} \\ \dfrac{\partial}{\partial\zeta} \end{bmatrix} = [\mathbf{J}] \begin{bmatrix} \dfrac{\partial}{\partial x} \\ \dfrac{\partial}{\partial y} \\ \dfrac{\partial}{\partial z} \end{bmatrix}. \tag{39}$$

It is also necessary to transform the integrand of Eq. (37) into the ξ, η, ζ coordinate system. Then,

$$[\mathbf{k}]=\int_{-1}^{+1}\int_{-1}^{+1}\int_{-1}^{+1}\mathbf{B}^{\mathrm{T}}\mathbf{D}\mathbf{B}|\mathbf{J}|\,d\xi\,d\eta\,d\zeta, \tag{40}$$

where $|\mathbf{J}|$ is the jacobian determinant.

In our calculations, the integration was carried out numerically using the gaussian quadrature formula of the order one ($n=2$) and the displacements of nodal points were approximated.

In the hexahedral element where the displacement function is defined as Eq. (38), the strain distribution is not assumed to be constant because the first derivative of u_x with ξ contains not only the invariant term but also variant terms corresponding to η and ζ. Therefore, we divided this hexahedral element into five tetrahedrons in two different ways as shown in **Fig. 6** (lower). In a tetrahedral element, the displacement function can be expressed as follows,

$$u_x=\alpha_1+\alpha_2 x+\alpha_3 y+\alpha_4 z, \tag{41}$$

where constant strains are implicitly assured. Then, strain components in the hexahedron are approximated by obtaining the mean value of ten calculations of constant strains in ten tetrahedrons involved in the hexahedron.

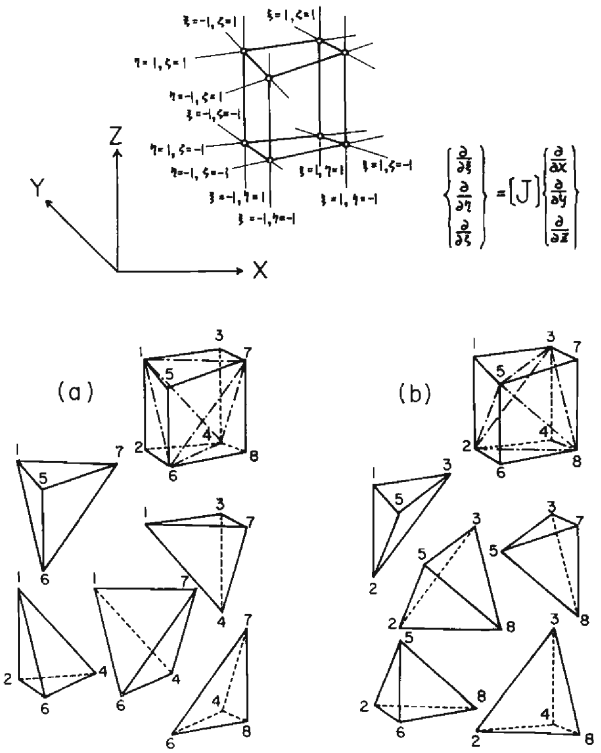

Fig. 6. Local skew coordinate system used for expressing the inclined hexahedron (upper) and two ways of dividing a hexahedron into five tetrahedrons (lower).

Before calculating $[T_{ij}]$ for the actual topography around the Amagase Observatory, the method and program were tested with four topographic models of simple structures as shown in **Fig. 7**. Models (1) and (2) are the hill and valley structures having a uniform cross-section in the y direction and models (3) and (4) are the three dimensional hill and valley structures where the topographic heights are smoothly varied toward x and y directions. Three independent loads were applied to these models; in the absence of topographic effects the first would have produced a uniform uniaxial strain e_1 in the x direction, the second a uniform shear strain e_2 with the principal axis at 45° to x and y axes, and the third a uniform uniaxial strain e_3 in the y direction. These boundary conditions are satisfied by specifying the nodal point displacements on the base and side boundaries of the structure. Poisson's ratio was assumed to be 0.25 for all elements.

Contour plots of T_{11} representing the response to the applied uniaxial strain e_1 at the ground surface are shown in **Fig. 7**. These results indicate that the strains observed on the ground at the center of the valley may be two times larger than the applied uniaxial strain and those observed on the top of the hill may be smaller than a factor of 0.2. At the valley margin, the strains are smaller than a factor of 1.0. On the contrary, at the foot of the hill, those are larger than a factor of 1.0.

Fig. 8 shows comparisons between values of T_{11} obtained from three-dimen-

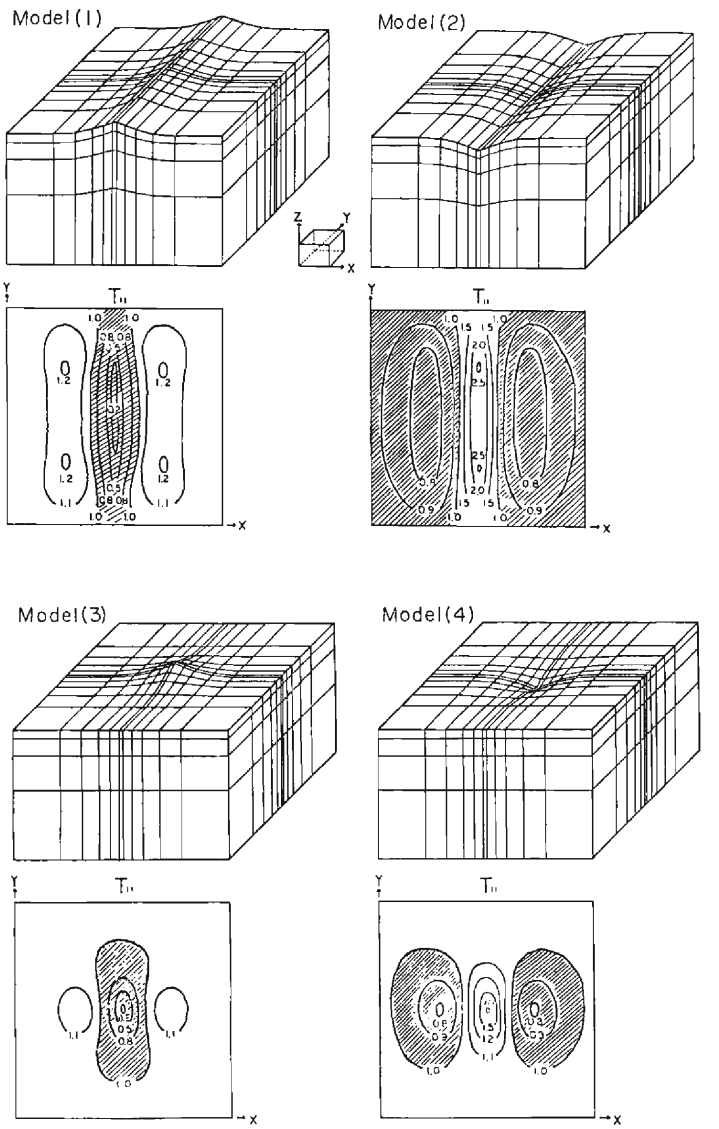

Fig. 7. Three-dimensional finite element models and contour plots of T_{11} for corresponding models.

sional calculations for models (1) and (2) in the x-z cross-section at $y=0$ (the right hand) and those obtained from two-dimensional calculations using triangular elements for the same profiles (the left hand). The values for a quadrilateral on the right hand is in any case nearly equal to the mean value for two triangles on the left hand corresponding to the quadrilateral. Based on these results, calculations of topographic effects for the actual structure around the Amagase Observatory were carried out using three-dimensional finite element techniques.

As shown in **Fig. 1** (upper), the topography of this area is characterized by the

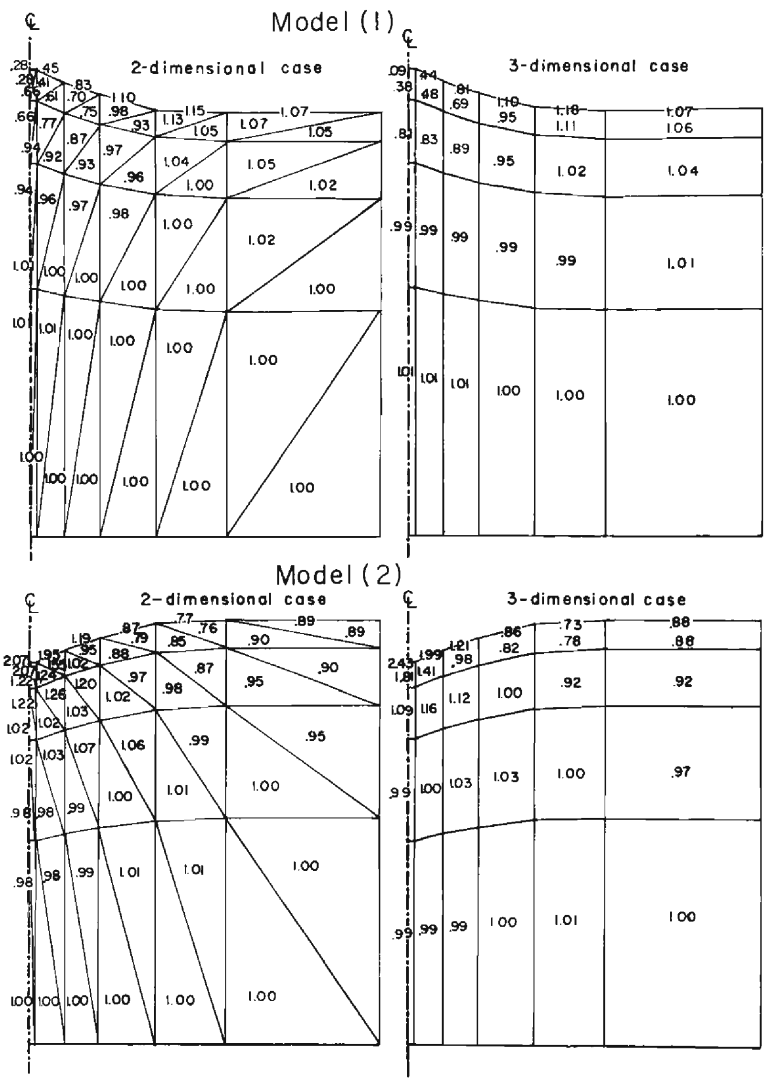

Fig. 8. Comparisons of two- and three-dimensional calculations for model (1) (upper) and model (2) (lower).

Uji-river which flows through highlands on the right hand into lowlands on the left hand of this figure. The observatory is located in the highland of Palaeozoic formations consisting of shale, clay-slate, chert and sand-stone (Ueji[39]). The region of 8 km $\times$ 8 km in the x-y plane and about 3 km in the z direction was divided into 484 ($11\times11\times4$) elements having the same material properties ($\lambda=2.18\times10^{10}$ N/m^2, $\mu=1.73\times10^{10}$ N/m^2, $E=4.49\times10^{10}$ N/m^2 and $\nu=0.279$). According to the procedure mentioned previously, values of $[T_{ij}]$ for this model were calculated. In **Fig. 9**, contour plots of T_{11}, T_{22} and T_{33} at the ground surface are shown, together with the three-dimensional finite element model. These plots reflect well character-

istics of local topography around the observatory. The dimension of the central element in the uppermost layer is 200 m × 200 m × 200 m. Values of T_{ij} are obtained for this element, in which our instruments are placed, as follows,

$$[T_{ij}]=\begin{bmatrix} 0.915 & -0.028 & -0.039 \\ -0.030 & 0.944 & -0.006 \\ -0.006 & 0.002 & 0.973 \end{bmatrix} \tag{42}$$

As a result, the topographic effect expected for the Amagase Observatory is not so much distinct as those expected for other observatories[15),16),17)]. Theoretically predicted tidal strains corrected with $[T_{ij}]$ are shown in **Table 7**.

If the surface is locally sloped, the normal stress σ_z, which should vanish at the

Table 7. Theoretically expected tidal strains containing the topographic correction.

	M_2 constituent		O_1 constituent	
	Amplitude ($\times 10^{-9}$)	Phase lag (degree)	Amplitude ($\times 10^{-9}$)	Phase lag (degree)
x-direction	5.69	−4.0	6.03	16.9
y-direction	9.97	4.6	4.50	−19.4

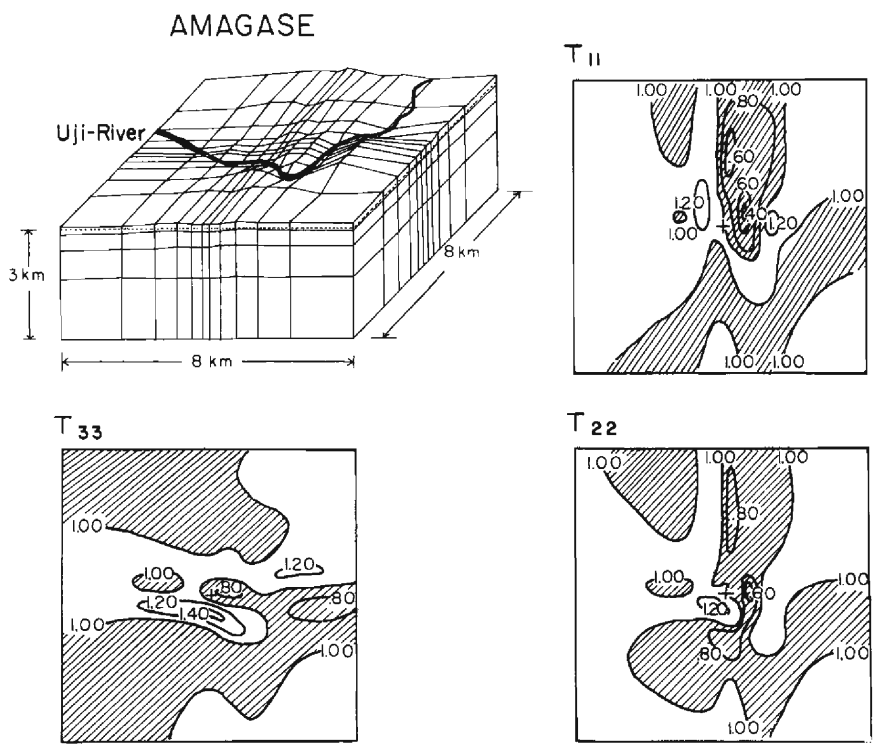

Fig. 9. Three dimensional finite element model around the Amagase Observatory and contour plots of T_{11}, T_{22} and T_{33}.

flat surface, is no longer assumed to be zero. We now estimate the values of σ_z induced by the topographic effect at the observation site. Strains and stresses applied at the boundary and those obtained from finite element calculations at the observation site are given in **Table 8** under three independent boundary conditions; I. $\sigma_z=\tau_{yz}=\tau_{zx}=0$, e_{xx}=unit strain, $e_{xy}=e_{yy}=0$, II. $\sigma_z=\tau_{yz}=\tau_{zx}=0$, $e_{xx}=0$, e_{xy}=unit strain, $e_{yy}=0$, III. $\sigma_z=\tau_{yz}=\tau_{zx}=0$, $e_{xx}=e_{xy}=0$, e_{yy}=unit strain. Values of σ_z calculated for the observation site are 4.0, 1.1 and 0.4% of Σ for conditions I, II and III, respectively. Where Σ is the total stress ($=\sigma_x+\sigma_y+\sigma_z$) which would produce the uniaxial unit strain in the principal direction in the absence of the topographic effect. In any case, the normal stress σ_z induced by the topographic effect does not exceed 4% of the applied stress. It is thus reasonable to neglect σ_z in treatment of cavity effects mentioned in section 3.

Table 8. Strains and stresses applied at the boundary and those obtained from finite element calculations for the observation site.

	e_{xx}	e_{yy} ($\times 10^{-9}$)	e_{zz}	σ_x	σ_y ($\times 10$ N/m^2)	σ_z	σ_z/Σ*
Condition I.							
A	1.0	0.0	−0.387	4.80	1.34	0.0	
B	0.915	−0.006	−0.308	4.48	1.29	0.247	0.040
Condition II.							
A	0.0	0.0	0.0	0.0	0.0	0.0	
B	−0.028	0.002	0.022	−0.11	−0.00	0.065	0.011
Condition III.							
A	0.0	1.0	−0.387	1.34	4.80	0.0	
B	−0.039	0.973	−0.366	1.10	4.61	0.027	0.004

A: Strains and stresses applied at the boundary.

B: Strains and stresses obtained from finite element calculations for the observation site.

* $\Sigma=4.80+1.34=6.14$

6. Geological Effects

In previous sections, cavity and topographic effects on tidal strain measurements have been approximated using finite element techniques. In addition to those, the lateral variations of elastic parameters caused by local geology may also deform the regional strain fields.

In regard to the lateral inhomogeneities, we have made electro-optical distance measurements of three base-lines aligned along the Amagase tunnel[40]. As shown in **Fig. 10**, strain accumulations obtained from these measurements exhibited the rates of (-2.6 ± 0.9), (-1.5 ± 0.5) and $(-1.6\pm0.2)\times10^{-6}$/year for base-lines having lengths of 0.4, 0.9 and 1.7 km, respectively. And the strain accumulation obtained from continuous records of the E–1 extensometer installed in the same direction exhibited the rate of -1.9×10^{-6}/year. Both results are consistent within the observational errors. As a result, lateral inhomogeneities of the strain along the tunnel in our observatory are considered to be small and we do not attempt at present time

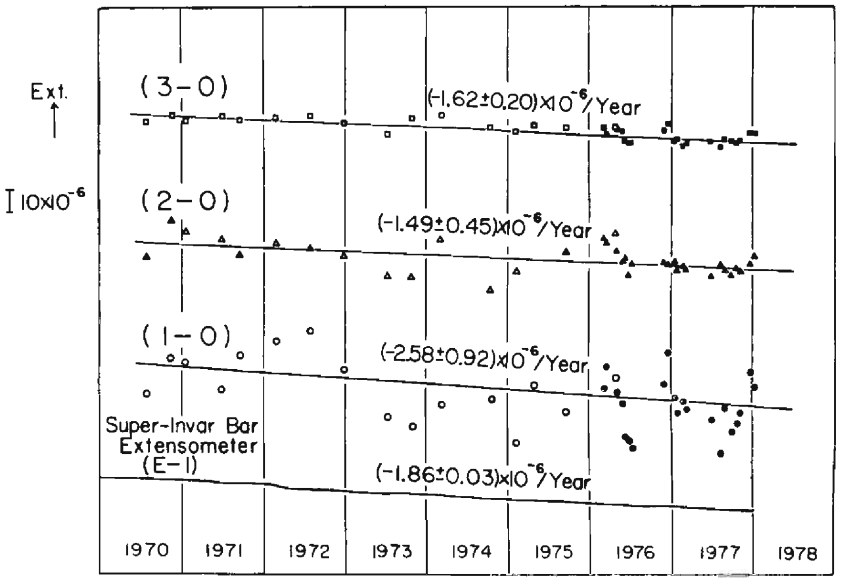

Fig. 10. Comparison of secular ground-strains obtained from electro-optical distance measurements of three base-lines in the Amagase tunnel and from the super-invar bar extensometer along the same direction.

to evaluate the geological effect using finite element techniques.

7. Comparison between Observed and Theoretically Predicted Tidal Strains

Taking the cavity and topographic effects into consideration, we compare the observed and theoretically predicted tidal strains of M_2 and O_1 constituents in both x and y directions (along and across the tunnel, respectively). Observed values eliminated the cavity effect and normalized with nodal parameters of the moon are shown as the mark **O** in **Fig. 11**, together with theoretically predicted tidal strains for a solid earth **E**, contributions from ocean tide loadings **L** and topographic effects **T**. Here we consider the sum of **E**, **L** and **T** to be theoretically expected tidal strains **S** at the Amagase Observatory. Comparing **O** and **S**, differences of phases between them are smaller than 5° in any case, but there still exist systematic differences between their amplitudes; the ratios of $|\mathbf{O}|$ and $|\mathbf{S}|$ in the x direction are $4.88/5.69=0.86$ for the M_2 constituent and $5.11/6.03=0.85$ for the O_1 constituent and those in the y direction are $13.29/9.97=1.33$ and $6.84/4.50=1.52$ for M_2 and O_1 constituents, respectively.

Then, we estimate errors inherent in each term. At first, estimations of **E** are considered to be accurate to within 2% in amplitude even if the assumed value of Love number varies from 0.6114 to 0.60. Secondly, as mentioned in section 4, values of **L**, which were calculated for the M_2 constituent using three independent sets of data of ocean tides, showed differences in their amplitudes of up to 0.7×10^{-9}. This may cause the error of about 10% in estimating the values of **S**. For the O_1

constituent, the error may be smaller than that for the M_2 constituent because the value of **L** in this case is one order smaller than that of the M_2 constituent. Thirdly, in order to check the accuracy of the topographic matrix $[T_{ij}]$, we have repeated the finite element calculation for an another model of the topography around the Amagase Observatory using the same procedure described in section 5. This model has a dimension of 5 km × 5 km × 3 km and it is divided into 484 elements. The smallest element at the center of the uppermost layer has a dimension of 100 m × 100 m × 200 m. Comparing results calculated for this model with those obtained previously for the model having the dimension of 8 km × 8 km × 3 km, the difference is within 6%. Finally, the error of **S** (=**E**+**L**+**T**) is estimated to be about 12%. In addition to it, the error caused by the calculation of cavity effects must be added for components of the y direction. Taking these errors into consideration, differences of amplitudes between **O** and **S** obtained for the x direction are comparable to the error but those obtained for the y direction is far larger than the error. It may be explained by the geological effect which has not been discussed in detail in this paper. But as the most possible source of these differences, we consider fluctuations of the level of the ground-water caused by meteorological changes and water level changes of the Amagase Reservoir existing near the observatory. This aspect we will discuss in a subsequent paper.

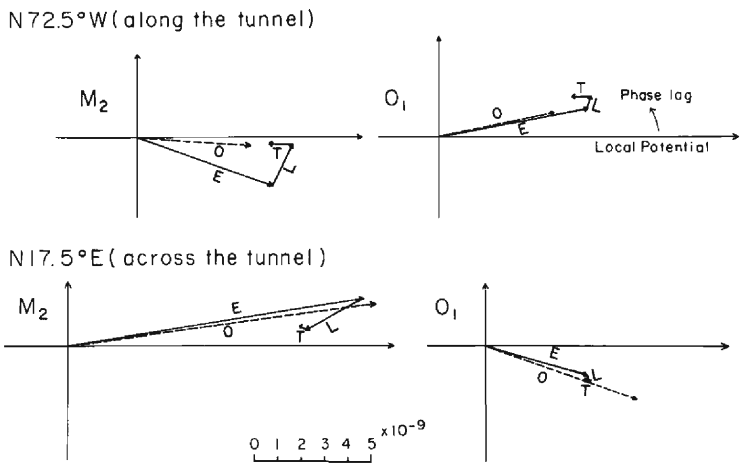

Fig. 11. Vector diagrams of M_2 and O_1 constituents.

E: Theoretically predicted value for the Gutenberg-Bullen A earth model.
L: Contribution from the ocean tide loading.
T: Topographic effect.
O: Observed tide.

8. Conclusion

Based on the tidal strain data obtained from extensometers with laser interferometer systems, effects of local inhomogeneities on tidal strain measurements have been investigated.

Tidal strain enhancements observed with the horizontal component across the

tunnel and the vertical component are explained well with the cavity effect calculated by two-dimensional finite element techniques for the actual cross-section of the horseshoe shaped tunnel.

After eliminating the cavity effect from the observed data, we have compared these values of M_2 and O_1 constituents with homogeneous tidal strains expected at Amagase. As a result, there remain systematic differences in their amplitudes. Then, we have investigated whether these differences can be explained by the topographic effect or not. Calculations have been made by three-dimensional finite element techniques in which the region of 8 km × 8 km × 3 km is expressed as an assembly of 484 hexahedral elements. Comparing the observed tidal strains with theoretically predicted ones containing the topographic correction, differences between their phases are within 5° in any case, and ratios of amplitudes are within 0.85~0.86 for the x direction (along the tunnel) and 1.33~1.52 for the y direction (across the tunnel). In the x direction, observed amplitudes are about 15% smaller than theoretically predicted ones but these differences are comparable to errors inherent in calculations. On the other hand, observed amplitudes in the y direction are 33~52% larger than theoretically predicted ones. These differences predominantly exceed error levels. As the most possible source of these differences, we consider the hydrological perturbation caused by fluctuations of the ground-water level around the observation tunnel. Effects of the hydrological perturbation on ground-strain measurements, especially those related to changes of the water level of the Amagase Reservoir will be discussed in detail in a subsequent paper.

Acknowledgements

The author wishes to express his thanks to Prof. Michio Takada and Dr. Tamotsu Furuzawa for their encouragement and helpful suggestions during the course of this work. The author is also grateful to Dr. Torao Tanaka for critically reading the manuscript to improve the present paper and for generous permission to make use of his computational results of loading effects of ocean tides. Thanks are also due to Mr. Masaru Yamada and Mr. Akio Hirono for their help in maintenance of instruments and to Mr. Masakuni Hashida for kindly offering his computational results of loading effects of ocean tides.

The computations involved were made partly with a FACOM M-140 at the Information Data Processing Center for Disaster Prevention Research, of the Disaster Prevention Research Institute, Kyoto University, and partly with a FACOM M-160AD at the Computing Center of the Institute for Chemical Research, Kyoto University.

References

1) Takemoto, S.: Laser interferometer systems for precise measurements of ground-strains, Bull. Disas. Prev. Res. Inst., Kyoto Univ., Vol. 29, Part 2, No. 262, 1979, pp. 65–81.
2) Berger, J. and R. H. Lovberg: A laser earth strain meter, Rev. Scient. Instr., Vol. 40, No. 12, 1969, pp. 1569–1575.
3) Levine, J. and J. L. Hall: Design and operation of a methane absorption stabilized laser strainmeter, J. Geophys. Res., Vol. 77, No. 14, 1972, pp. 2595–2609.
4) Goulty, N. R., G. C. P. King and A. J. Wallard: Iodine stabilized laser strainmeter, Geophys.

J. R. astr. Soc., Vol. 39, 1974, pp. 269–282.
5) King, G. C. P. and R. G. Bilham: Tidal tilt measurement in Europe, Nature, Vol. 243, 1973, pp. 74–75.
6) Itsueli, U. J., R. G. Bilham, N. R. Goulty and G. C. P. King: Tidal strain enhancement observed across a tunnel, Geophys. J. R. astr. Soc., Vol. 42, 1975, pp. 555–564.
7) Ozawa, I.: Observations of tidal strains at Osakayama Observatory, Part II. Annuals Disas. Prev. Res. Inst., Kyoto Univ., No. 10A, 1967, pp. 63–75 (in Japanese).
8) Melchior, P., B. Ducarme, J. M. Van Gils, J. Flick and C. Denis: Preliminary results obtained with a vertical strainmeter at the underground laboratory of geodynamics at Walferdange (Grand-duchy of Luxembourg), Phys. Earth and Planetary Interiors, Vol. 9, 1974, pp. 97–100.
9) Harrison, J. C.: Cavity and topographic effects in tilt and strain measurement, J. Geophys. Res., Vol. 81. No. 2, 1976, pp. 319–328.
10) Blair, D.: Topographic, geologic and cavity effects on the harmonic content of tidal strain, Geophys. J. R. astr. Soc. Vol. 48, 1977, pp. 393–405.
11) Blair, D.: Topographic effects on the tidal strain tensor, Geophys. J. R. astr. Soc., Vol. 46, 1976, pp. 127–140.
12) Tanaka, T. and P. Sydenham: The M_2 earth tides at Cooney Geophysical Observatory in Armidale, Eastern Australia, Proceedings of the 8th International Symposium on Earth Tides, 1977, pp. 510–529.
13) Emter, D., A, Jensch and H. Kiesel: Finite element estimates of elastic effects on tidal tilt and strain with special respect to results from the Schiltach Observatory, Proceedings of the 8th International Symposium on Earth Tides, 1977, pp. 434–450.
14) Ooe, M. and T. Sato: On the topographic and cavity effects on the observation of the earth tides, Abstract of the 54th General Meeting of the Geodetic Society of Japan, 1980, pp. 14–15 (in Japanese).
15) Levine, J. and J. C. Harrison: Earth tide strain measurements in the Poorman mine near Boulder, Colorado, J. Geophys. Res., Vol. 81, No. 14, 1976, pp. 2543–2555.
16) Berger, J. and C. Beaumont: An analysis of tidal strain observations from the United States of America, II. The inhomogeneous tide, Bull. Seism. Soc. Amer., Vol. 66, No. 6, 1976, pp. 1821–1846.
17) Hashida, M. and K. Shigetomi: Topographic effects on the earth tidal strains at Osakayama, J. Geodetic Soc. Japan, Vol. 27, No. 1, 1981, pp. 11–21 (in Japanese).
18) Latynina, L. A.: On possibility of studies of fault in the Earth's crust from the process of tide deformation, Izv. Acad. Sc. USSR, Earth Phys., No. 3, 1975, pp. 16–26 (in Russian).
19) Latynina, L. A. and S. D. Rizaeva: About variations of tidal deformations before earthquakes, Izv. Acad. Sc. USSR, Earth Phys., No. 9, 1975, pp. 84–87 (in Russian).
20) Latynina, L. A. and T. P. Shishkina: About intensity of tidal and tectonic motions in the zone of the Surhob fault, Izv. Acad. Sc. USSR, Earth Phys., 1978, No. 6, pp. 87–93 (in Russian).
21) Latynina, L. A.: About tidal deformations at the Chusal station, Tadzhikskaya SSR, Study of Earth Tides, Nauka, Moscow, 1980, pp. 207–214 (in Russian).
22) King, G. C. P.: The siting of strainmeters for teleseismic and tidal studies. Recent Crustal Movements, R. Soc. N. Z. Bull., Vol. 9, 1971, pp. 239–247.
23) King, G. C. P. and R. G. Bilham: Strain measurement instrumentation and technique, Phil. Trans. R. Soc. Lond. A, Vol. 274, 1973, pp. 209–217.
24) Bilham, R. G., G. C. P. King and D. P. McKenzie: Inhomogeneous tidal strains in Queensbury tunnel, Yorkshire, Geophys. J. R. astr. Soc., Vol. 37, 1974, pp. 217–226.
25) Evans, R., J. Beavan, R. G. Bilham and G. C. P. King: A survey of earth strain tides in Great Britain, Geophys. J. R. astr. Soc., Vol. 57, 1979, pp. 119–135.
26) Major, M. W., G. H. Sutton, J. Oliver and R. Metsger: On elastic strain of the earth in the period range 5 seconds to 100 hours, Bull. Seism. Soc. Amer., Vol. 54, 1964, pp. 295–346.
27) Panek, L. A.: Calculation of the average ground-stress components from measurements of

the diametral deformation of a drill hole, Testing Techniques for Rock Mechanics, ASTM STP 402, Am. Soc. Testing Mats., 1966, pp. 106–132.

28) Sokolnikoff, I. S.: Mathematical theory of elasticity, McGraw-Hill Book Co., New York, 1965.

29) Zeinkiewicz, O. C.: The finite element method in engineering science, McGraw-Hill Book Co., 1971.

30) Akamatsu, J., T. Furuzawa and K. Irikura: On natures of S waves from local small earthquakes observed at Amagase Crustal Movement Observatory, Annuals Disas. Prev. Res. Inst., No. 18 B, 1975, pp. 11–21 (in Japanese).

31) Melchior, P.: The tides of the planet earth, Pergamon Press, 1978.

32) Nakano, M.: Choseki-gaku (Harmonic analysis and prediction of tides), Kokin-shoten, Tokyo, 1940 (in Japanese).

33) Farrell, W. E.: Deformation of the earth by surface loads, Rev. Geophys. and Space Phys., Vol. 10, No. 3, 1972, pp. 761–797.

34) Ogura, S.: The tides in the seas adjacent to Japan, Bull. Hydrograph. Dep., Vol. 7, 1933, pp. 1–189.

35) Navy, Ministry of Defence, USSR: *ATAAC OKEAHOB*, Pacific Ocean, 1974 (in Russian).

36) Navy, Ministry of Defence, USSR: *ATAAC OKEAHOB*, Atlantic and Indian Oceans, 1977 (in Russian).

37) Hendershott, M. C.: The effects of solid earth deformation on global ocean tides, Geophys. J. R. astr. Soc. Vol. 29, 1972, pp. 389–402.

38) Beaumont, C. and J. Berger: An analysis of tidal strain observations from the United States of America, I. The laterally homogeneous tide, Bull. Seism. Soc. Amer., Vol. 65, No. 6, 1975, 1613–1629.

39) Ueji, T.: Kyōto kinbō chishitsu-shi (Geological history in and around Kyoto), Chikashigen-kenkyūsho, Kyoto, 1961 (in Japanese).

40) Fukuzawa, T., S. Takemoto and K. Onoue: Electro-optical distance measurements in Kiniki, Chugoku and Shikoku districts (1974–1978), J. Geodetic Soc. Japan, Vol. 24, No. 3, 1978, pp. 132–140 (in Japanese).